Modeling mass and density distribution effects on the performance of co-extruded electrodes for high energy density lithium-ion batteries
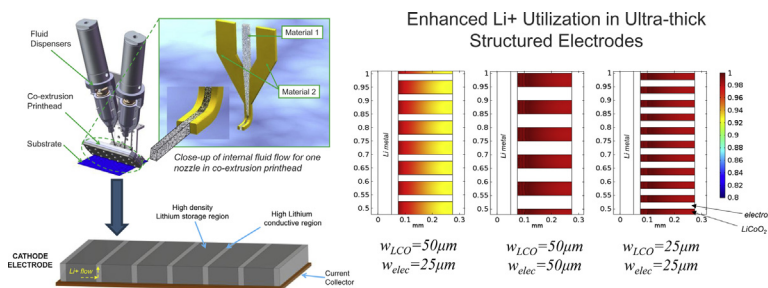
CrossMark

Corie L. Cobb [a,*], Mario Blanco [b]

[a] Palo Alto Research Center (PARC), Hardware Systems Laboratory, 3333 Coyote Hill Road, Palo Alto, CA 94043, USA
[b] King Abdullah University of Science & Technology (KAUST), Innovation Cluster, Thuwal 239556900, Saudi Arabia

HIGHLIGHTS

- Two-dimensional finite element analysis performed on structured battery electrodes.
- Thick co-extruded LiCoO$_2$ electrodes enable a substantial improvement in energy.
- 25–100 μm width electrode fingers garner best performance at a 1C rate.
- Co-extruded electrode structures fundamentally minimize the ionic pathway for Li$^+$.

GRAPHICAL ABSTRACT

ARTICLE INFO

ABSTRACT

Utilizing an existing macro-homogeneous porous electrode model developed by John Newman, this paper aims to explore the potential energy density gains which can be realized in lithium-ion battery electrodes fabricated with co-extrusion printing technology. This paper conducts an analysis on two-dimensional electrode cross-sections and presents the electrochemical performance results, including calculated volumetric energy capacity for a general class of lithium cobalt oxide (LiCoO$_2$) co-extruded cathodes, in the presence of a lithium metal anode, polymer separator and liquid ethylene carbonate, propylene carbonate, and dimethyl carbonate (EC:PC:DMC) electrolyte. The impact of structured electrodes on cell performance is investigated by varying the physical distribution of a fixed amount of cathode mass over a space of dimensions which can be fabricated by co-extrusion. By systematically varying the thickness and aspect ratio of the electrode structures, we present an optimal subset of geometries and design rules for co-extruded geometries. Modeling results demonstrate that ultra-thick LiCoO$_2$ electrodes, on the order of 150–300 μm, can garner a substantial improvement in material utilization and in turn capacity through electrolyte channels and fine width electrode pillars which are 25–100 μm wide.

1. Introduction

Lithium-ion batteries, in which lithium ions shuttle between an insertion cathode and anode, have emerged as the power source of choice for consumer electronics and high performance rechargeable batteries [1]. Thin film lithium-ion batteries have the potential to reach energy densities as high as 1000 Wh l^{-1} (250 Wh kg^{-1}), power densities around 2500 W kg^{-1}, and high life cycles (> 1000) [2]. In addition, thin film batteries have demonstrated good temperature stability at temperatures ranging from $-40\,^\circ$C to 150 $^\circ$C. Given these advantages, one may conclude that building battery stacks of thin film electrodes will enable high performance, high energy density lithium-ion batteries. However, the need to add

* Corresponding author. Tel.: +1 650 812 4000; fax: +1 650 812 4251.
E-mail addresses: corie.cobb@parc.com (C.L. Cobb), mario.blanco@kaust.edu.sa (M. Blanco).

current collectors, separators, and other inactive components for each cell layer makes this impractical. These inactive components contribute significantly to a battery stack's mass and volume (over 50%) but not to the active electrode material. A large surface area is required for thin film batteries in order to have sufficient electrode material, especially for high discharge capacities. State of the art high power lithium-ion microbatteries with interdigitated three-dimensional nanoporous electrodes solve some of the aforementioned problems, by reducing the stack of multiple inactive components, but introduce other issues such as high manufacturing costs and trade-offs between power and energy density [3].

As an alternative to thin film batteries, one can build ultra-thick battery electrodes which provide large amounts of energy or power for a given discharge rate. However, this approach is limited by diffusion controlled lithium-ion (Li$^+$) intercalation, especially at high discharge rates. Ultra-thick battery anodes [4] and the electrochemical properties of ultra-thick LiCoO$_2$ cathodes prepared by screen-printing techniques [5] have been considered for high discharge capacities. However, this direction does not consider the fact that for all but the thinnest cathodes, or very low current densities, discharge capacities from 4.2 to 3.0 V are limited by the lithium diffusivity in Li$_x$CoO$_2$ and the ultimate formation of a resistive layer at the interface as the state of discharge (x) approaches 1.0. Measurements of the equilibrium open circuit potential and ac impedance upon deep discharge support this model [6].

Promoting higher diffusion for the $0.96 < x < 1.0$ phase in LiCoO$_2$ can greatly enhance the power and energy achievable by both thin film and ultra-thick batteries. However, this enhancement often requires doping and fine crystallization control of the cathode material in question to generate the required high ion diffusion at high states of charge [6]. Alternatively, reducing the lithium-ion diffusion pathway, while providing sufficient cathode mass for high discharge capacities, may significantly alleviate the problems encountered with thin film and ultra-thick electrodes. The main issue becomes how to best distribute the required mass or density of any given amount of electrochemically active material to reach the full potential of a given electrode.

Both thin film and ultra-thick electrodes offer distinct advantages but fail to yield optimal performance. Can more active material be utilized in an ultra-thick lithium-ion battery while keeping the advantages of a thin film battery? We believe the answer lies in understanding how, for a constant amount of cathode material, mass and density spatial distributions affect the performance of lithium-ion batteries. This work presents solutions, using computational results that include electrolyte diffusivity in porous media, tortuosity effects, with a systematic search for optimal mass and density distribution in LiCoO$_2$ cathodes fabricated by co-extrusion [7].

1.1. Three-dimensional (3D) battery electrodes

1.1.1. Experimental and computational studies

The benefits of expanding the dimensionality of electrochemically active material from flat to more complex geometries have been the focus of recent research with many researchers exploring a wide variety of geometries and fabrication methods. Three-dimensional (3D) battery structures significantly increase electrode surface area and in turn increase energy storage capacity. 3D batteries have the potential to transform the performance of a multitude of battery systems through structural changes rather than material changes. Any advances in new materials can always be incorporated into 3D structured batteries.

Experimentally, researchers have been investigating the benefits of 3D battery electrodes. A super ink jet printing (SIJP) system was used by Ho et al. to fabricate alkaline zinc−silver micro-batteries with electrode pillar structures [8]. The fabricated electrode pillars were on the order of 40 μm tall and 10 μm in diameter located approximately 100 μm apart. The 3D electrode structures demonstrated a 60% increase in areal capacity compared to planar electrodes of a similar footprint area. Baggetto et al. explored the advantages of 3D negative electrode stacks with a micro-pore channel configuration for a solid-state battery [9,10]. This design gave a unique surface area increase over a standard battery. The authors found that further optimization of the trench dimensions ideally result in a storage capacity increase of more than five times with respect to planar electrode films. Lastly, focusing on a form of extrusion technology, micro pore channel battery structures have also been fabricated [11]. By creating a periodic pore channel array in an electrode, Bae et al. were able to reduce the effective tortuosity of an LiCoO$_2$ electrode which in turn helped retain greater capacity at higher discharge rates in thick electrodes (up to 220 μm) with pore channels for electrolyte approximately 5 μm in diameter when compared with a conventional electrode. All of the aforementioned experimental efforts demonstrate the advances of 3D structures electrodes. However, no systematic search for optimal geometries was conducted in any of these cases.

Focusing on computational modeling, researchers have also investigated the effects of 3D battery structures. Interdigitated anode and cathode electrode structures have been studied by Garcia et al. [12]. The microstructures considered consisted of a highly tortuous particle distribution with a topology of ordered branches of electrode material. Simulations of micro-structured interdigitated batteries show that the power density of a rechargeable battery can be engineered by maximizing the electrochemical driving force for intercalation while decreasing the ion transport distances of the material components. At high discharge rates, energy improvements around 37% were realized with the aforementioned structures. Zadin et al. [13] conducted finite element modeling (FEM) of electrode material utilization in a 3D microbattery structure with interdigitated anode and cathode electrodes − similar to other 3D interdigitated structure concepts [12,14]. The authors examined the influence of electrical conductivity and electrode pillar height on the overall performance of the battery. Issues with inhomogeneous lithiation were found due to differences in surface area between electrode pairs which caused non-uniform current density distributions. Zadin et al. [15] extended the aforementioned work and examined the impact of further varying the material properties and geometry profiles of the interdigitated electrode structures. It was shown that the locally high non-uniform current densities where reduced when sharp points and corners in the geometry were rounded, leading to more uniform ion concentration gradients. At the micro-scale, Smith et al. used experimentally derived cross sections of rechargeable lithium ion batteries to computationally model the effect of microstructure on the galvanostatic discharge of a LiCoO$_2$|LiC$_6$ cell [16]. This highly detailed level of analysis demonstrated that large inhomogeneous particle distributions led to diminished macroscopic power densities which limit the response of a lithium-ion cell. Though these computational studies provide a meaningful window into the benefits of 3D electrode structures, the important issue of mass and density distribution of the electrode remains unexplored.

1.1.2. 3D battery design principles

Design principles for 3D batteries typically focus on the geometrical and material requirements of the electrodes. Estimates of performance for 3D battery architectures indicate that an increase in the height of an interdigitated 3D battery pillar, L, results in increased energy capacity and electrode area, without an

increase in transport distances. Dependence of electrode utilization (U) on electrode conductivity (σ) and electrolyte ion mobility (μ) for interdigitated rectangular cross-section electrodes are represented, by the dimensionless number $U = (w^2/L^2)(\sigma/\mu)(1/C)$ where w is the width of the electrode pillar and C is the volumetric energy capacity (C cm^{-3}) [14]. U yields a measure of current uniformity across the 3D electrode surfaces if the volumetric energy capacity C is known. U embeds in a single parameter a measure of how well the electrode material is uniformly utilized during cell charging and discharging. Decreasing U leads to a more uniform current distribution along the length of the electrode. Increasing U corresponds to a more non-uniform discharge of the electrodes, which may result in underutilization of the electrode material during fast discharge rates as well as increasing stress along the length of the electrodes.

Roberts et al. [17] examine the advantages of 3D electrodes and highlight the dominating factors which impact the power and energy density of an electrode. The authors note that interdigitated anode and cathode electrodes help increase power density by minimizing ionic path lengths. In standard monolithic electrodes, Roberts et al. estimate that the given power per footprint area (P_A) can be represented by the following expression: $P_A \sim (1.5E_A D_{Li})/L^2$. E_A is the specific energy, D_{Li} is the diffusion coefficient for lithium ions in the solid phase, and L is the electrode thickness. Increasing L will at some point lead to performance limitations due to slow lithium ion diffusion, limiting the ability to deliver high energy and power simultaneously in thick monolithic electrodes. The structure of 3D batteries allows for fewer current collectors in the stack, which favors a higher volumetric density, as well as a double migration path for ions (to each of two surrounding electrodes) during charge and discharge, which favors power density. Both Long et al. [14] and Roberts et al. [17] emphasize that the height of the electrode pillar plays a strong role in determining the energy and power density of a 3D battery.

Because self-organization from an electrode slurry imposes limits on the experimental realization of new architectures, in this work we ask how co-extruded fabricated electrodes, as opposed to self-organized particle electrodes [3], perform as a function of mass and density spatial distribution for a fixed total mass of active electrode material.

2. Co-extruded electrodes

2.1. Co-extrusion electrode fabrication technology

A method of co-extrusion of dissimilar materials has been developed [7] to successfully produce high aspect ratio structures for battery electrodes in a cost-effective manner. The co-extrusion process is capable of direct deposition of features as small as 1–10 μm with aspect ratios ranging from 1 to 5 or greater with highly loaded pastes at print speeds up to 200 mm s^{-1}. Dispense needles [11] are suitable for prototype and laboratory scale printing but are impractical in a high-volume production setting due to the high operating pressures needed to push paste through a long narrow nozzle for fast processing speeds.

As shown in Fig. 1, a co-extrusion printhead assembly typically consists of a layered nozzle structure sandwiched between two plate structures which are then tightly sealed with clamping bolts. Each plate guides one of two extrusion materials from respective inlet ports to the layered nozzle structure which consists of a converging fluid path that helps minimize pressure drop. The concept of hydrodynamic focusing [18,19] is employed to minimize pressure drop, enabling two or more fluid streams to be narrowed into fine line features. During the co-extrusion process, the printhead is oriented at 45° relative to a substrate (i.e. a current collector foil in the case of batteries). Material 1 (which is the main battery
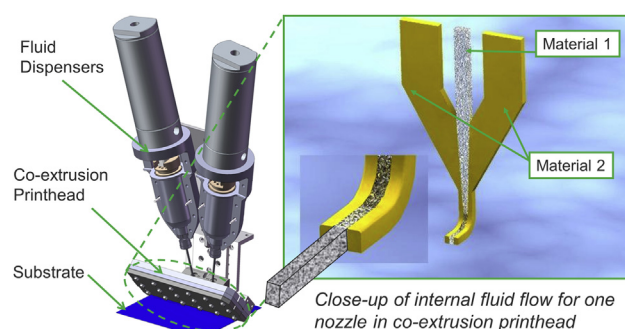

Fig. 1. Co-extrusion process.

electrode material in the case of this study) is directed towards the substrate as it moves beneath the printhead while Material 2 shapes Material 1 into tall and narrow electrode structures. The substrate is then heated to the necessary temperature to remove Material 2, leaving behind only Material 1. The high viscosity electrode material coupled with the printhead design ensures laminar flow regimes, and the extruded structure largely retains the shape formed in the nozzle orifice during extrusion. The relative thicknesses, widths, and lengths of the deposited features are dependent on the internal printhead geometry, fluid rheology, and printing process conditions. Depending on the desired electrode dimensions, the fluidic stack of nozzles can easily be exchanged for a multitude of alternate designs in order to achieve the necessary extruded electrode dimensions. Co-extrusion offers a mode of manufacturing with scale-up advantages for the fabrication of electrodes of varying mass and density distribution.

2.2. Co-extrusion electrode geometries

The co-extrusion technology mentioned in Section 2.1 allows one to utilize one or more electrode materials in a structured pattern. Unlike prior research, which has focused on interdigitated anode and cathode structures [12–15], we have chosen to focus on structuring a single electrode (see Fig. 2). Fig. 2 shows a two material example for a cathode electrode. One cathode material can be a high density lithium storage region while the second cathode material can enhance ionic conductivity and lithium diffusivity by having highly porous electrode material regions or sacrificial material which is evaporated to leave behind empty space for electrolyte. By structuring an electrode with conductive regions which are interleaved with storage regions, current paths can be shortened without compromising the capacity of an electrode. Although Fig. 2 shows only a cathode structure, nothing prevents the same geometry structure from being applied to the anode. Conventional battery electrodes are typically 40–90 μm in thickness and are fabricated by coating a layer of electrode material onto a metal sheet. These thin electrode batteries deal with a tradeoff between energy and power as thin electrodes help reduce ion transport distances but they simultaneously lower the capacity of a cell. Thickness limitations on thin electrodes are due to low diffusivity in
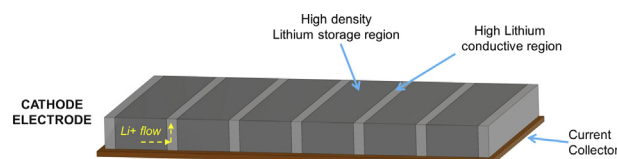

Fig. 2. Co-extruded cathode electrode. Lithium-ion flow shown for charging.

the solid phase (typically on the order of 10^{-10} to 10^{-8} cm^2 m^{-1} [20]). By co-extruding thicker (150 μm or greater) structured electrodes with electrolyte regions of high ion conductivity which help increase the effective conductivity, we can realize higher energy densities without limiting performance at high discharge rates. Many have observed that by restructuring battery electrodes, these inherent tradeoffs can be diminished [14].

2.3. Electrode design exploration

We utilize a macro-homogenous porous electrode model in COMSOL® [21] to investigate various co-extruded configurations for the porous cathode electrode of a battery made with LiCoO$_2$. Although a multitude of new battery materials have emerged over the last twenty years, LiCoO$_2$ is still a widely studied and utilized material. Thus, for the purposes of understanding the performance of co-extruded electrodes, LiCoO$_2$ was deemed a suitable material choice for a parametric study. By leveraging the COMSOL software platform, we can focus on the influence of geometrical parameters on the electrochemical and transport properties of co-extruded electrodes with FEM. A half-cell structure is employed with a 50 μm thick lithium metal anode, a 25 μm thick polymer separator, and a LiCoO$_2$ cathode (see Fig. 3a). This paper presents a geometric study on the cathode only, but the design principles can be extended to the anode as well. Each half-cell representation in COMSOL is a pseudo 3D model where the geometry is varied in the x and y dimensions, and the z dimension is a fixed value.

The cathode is parameterized as shown in Fig. 3b. We start with a fixed amount of porous cathode material mass which is sized 1.0 mm by 1.0 mm by 0.3 mm. The porous cathode electrode material consists of 52% LiCoO$_2$, 14.2% filler (a combination of binder and carbon), and 33.8% porosity by volume. Throughout each model, we hold the z-dimension fixed at 1 mm and vary the x and y-dimensions of the overall electrode while conserving cathode material mass. Conserving mass between models allows us to understand how for a given amount of porous electrode material, co-extruded structures can potentially change and improve transport properties in thick electrodes while also understanding the impact to energy density, otherwise any changes in energy density will be confounded by changes in total cathode material mass. The cathode is constructed with a varying number (n) of co-extruded columns of width $= w_{LCO}$ and height $= h$. In between each pillar of LiCoO$_2$ there is a region of electrolyte which will have the same height as the electrode, but a different width, w_{elec}. In Sections 3 and 4, we present a systematic analysis of the effect on discharge performance for a constant mass of porous electrode material, distributed over the space of possible electrode geometries which can be fabricated by co-extrusion.
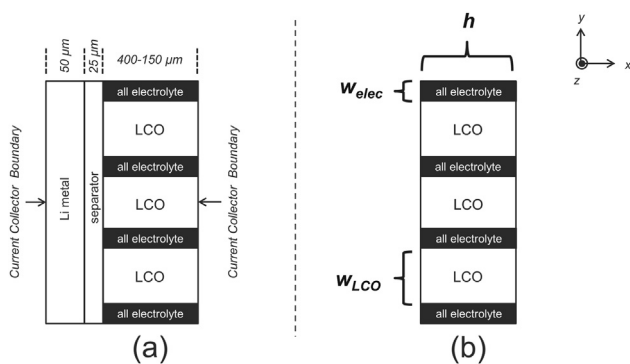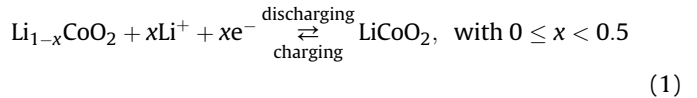

Fig. 3. (a) Representative geometry of a two-dimensional lithium battery with a co-extruded cathode; (b) a parameterized schematic of the cathode electrode only.

3. Model setup and methodology

John Newman and his research group conducted foundational work on mathematical models for lithium-ion batteries based on porous electrode theory [22–26]. These models have been extended over the years and are utilized widely to study the performance gains and potential failure modes of various lithium-ion battery systems. Many commercial tools which integrate Newman's model primarily adhere to the 1-dimensional (1D) isothermal porous electrode setup, similar to the original DUALFOIL program [22–24]. COMSOL [21] is one of the few commercially available multi-physics modeling packages with 3D FEM capability for solving transient electrochemistry problems. COMSOL integrates FEM with macro-homogeneous porous electrode theory enabling one to model two and three dimensional battery electrode structures, a feature not available in many modeling tools today [27]. For the electrode structures presented in Figs. 2 and 3, 1D mathematical models are not sufficient for exploring the range of performance gains potentially realized with co-extruded electrodes. It is for this reason that we use COMSOL's FEM battery package to iterate through various parameterizations of co-extruded cathode structures to better understand the potential energy density and power density benefits.

3.1. Model theory

In the following section, the theory for the lithium battery model is summarized. The detailed equations can be found in prior work by Doyle et al. [22–24]. At a high level, the battery model is based on charge balances in the electrolyte and electrodes, and mass balances for the salt and lithium in the cell. As we employ a lithium half-cell setup to study the cathode only, the electrochemical reaction for lithium cobalt oxide can be summarized by Equation (1).

$$\text{Li}_{1-x}\text{CoO}_2 + x\text{Li}^+ + x\text{e}^- \underset{\text{charging}}{\overset{\text{discharging}}{\rightleftarrows}} \text{LiCoO}_2, \text{ with } 0 \leq x < 0.5 \tag{1}$$

In the solid phase for the lithium insertion material, Ohm's law (2) defines the current density, i_s, as a function of the electrical conductivity, σ_s, and the gradient of the electric potential, ϕ_s.

$$i_s = -\sigma_s \nabla \phi_s \tag{2}$$

The potential of the solution phase (electrolyte) is defined by an extended Ohm's law (3) while a mass balance for the lithium ions in the solution phase is governed by Equation (4).

$$i_l = -\kappa_{l,eff} \nabla \phi_l + \frac{2\kappa_{l,eff}RT}{F}\left(1 + \frac{\partial \ln f}{\partial \ln c_l}\right)(1 - t_+)\nabla \ln c_l \tag{3}$$

$$\varepsilon_l \frac{\partial c_l}{\partial t} = \nabla \cdot \left(D_{l,eff}\nabla c_l\right) + \left(\frac{ai_{loc}}{F}\right)(1 - t_+) \tag{4}$$

In Equation (3), $\kappa_{l,eff}$ denotes the effective electrolyte conductivity, f the activity coefficient for the salt, t_+ the transport number for lithium ions, and c_l the electrolyte salt concentration while R is the universal gas constant. In the mass balance for the salt (4) ε_l describes the electrolyte volume fraction, $D_{l,eff}$ is the electrolyte salt diffusivity, and F is the faraday constant. The faradaic transfer of charge from the electrode to the electrolyte interface can be described by the Butler–Volmer relationship, where the local charge transfer current density (i_{loc}) is given as Equation (5):

$$i_{loc} = i_0 \left[e^{\left(\frac{\alpha_a F \eta}{RT} \right)} - e^{\left(-\frac{\alpha_c F \eta}{RT} \right)} \right] \qquad (5)$$

Faraday's law in Equation (6) relates the pore wall flux (j_n) to the divergence of the electrolyte phase current, i_l. The specific interfacial area of the electrode material is calculated by $a = 3\varepsilon_s/r$, where ε_s represents the volume fraction of active material and r_p is average particle radius.

$$a j_n = \frac{a i_{loc}}{F} = \frac{\nabla \cdot \boldsymbol{i_l}}{F} \qquad (6)$$

In Equation (7), i_0 denotes the exchange current density which is included as a source or sink term in the charge balances in porous electrodes. α_a is the anodic charge transfer coefficient, and α_c is the cathodic charge transfer coefficient, while k_a and k_c denote the anodic and cathodic reaction rates, respectively. $c_{s,max} - c_s$ represents the concentration of empty sites at the surface of the cathode particles, while c_l represents the salt concentration.

$$i_0 = F(k_c)^{\alpha_a}(k_a)^{\alpha_c}(c_{s,max} - c_s)^{\alpha_a}(c_s)^{\alpha_c}(c_l)^{\alpha_a} \qquad (7)$$

In Equation (8), η is the surface overpotential term. U denotes the open circuit potential, which in the case for LiCoO$_2$ is calculated using a piecewise cubic polynomial fitted to data from Ref. [28], ϕ_s the electrode potential and ϕ_l the electrolyte potential. Potential

losses due to a resistive film build up on the electrode particles are assumed to be 0 for the purposes of this design exploration.

$$\eta = \phi_s - \phi_l - U \qquad (8)$$

Assuming, isotropic spherical particles and no volume change in the cathode material is present, mass transport in a solid LiCoO$_2$ particle can be described by Fick's second law of diffusion (9). The boundary conditions are given in Equations (10) and (11) where r_p is the average radius of the particle.

$$\frac{\partial c_s}{\partial t} = \nabla \cdot (D_s \nabla c_s) \qquad (9)$$

$$\frac{\partial c_s}{\partial r} = 0|_{r=0} \qquad (10)$$

$$-D_s \frac{\partial c_s}{\partial r} = j_n|_{r=r_p} \qquad (11)$$

3.2. Material properties

An EC:PC:DMC electrolyte is assumed in the model based on parameters from Zhang et al. [29] and Valoen et al. [30]. Electrolytes are complex and play a vital role in the performance of lithium-ion batteries. Valoen et al. conducted an experimental study on Li$^+$ salt diffusion in the electrolyte (D_l), the conductivity (κ_l), and salt activity (f) for LiPF$_6$ in an ethylene carbonate (EC), propylene carbonate (PC) and dimethyl carbonate (DMC) mixture. Those properties are utilized in the model presented in this paper (Equations (12)–(14)), and the additional material parameters employed are summarized in Table 1.

$$\log(D_l) = -4.43 - \frac{54}{T - 5 \times 10^3 c_l - 229} - 0.22 \times 10^3 c_l \qquad (12)$$

$$\kappa_l = c_l \Big(-10.5 + 0.074T - 6.96 \times 10^{-5}T^2 + 668c_l$$
$$-17.8c_l T + 0.028 c_l T^2 + 4.94 \times 10^5 c_l^2 - 886c_l^2 T \Big)^2 \qquad (13)$$

$$f = 0.601 - 7.59c_l^{1/2} + 3.1 \times 10^4(2.53 - 0.0052T)c_l^{1/2} \qquad (14)$$

Park et al. report on the large spread of solid phase diffusivity values for LiCoO$_2$ (10^{-13}–10^{-7} cm^2 s^{-1}) [20]. The solid phase diffusivity is used to calculate how the Li$^+$ concentration field (c_s) changes with time which is critical to calculating a battery's capacity. For this reason, many researchers have prepared thin films of pure LiCoO$_2$, without the presence of a polymer binder and carbonaceous powders, by various methods to study fundamental kinetic parameters, such as lithium diffusivity, charge–discharge curves, and voltage versus state of charge. Jang et al. fabricated solid state batteries with sputtered LiCoO$_2$ films to understand how the solid phase diffusion rate varies as a function of state of charge [31]. It was found that the diffusion coefficient monotonically increases with decreasing state of charge values between 0.55 and 0.7, but then varies in a more complex manner near a state of charge of 0.5. We utilized this diffusivity versus state of charge relationship in order to capture the Li$^+$ diffusivity behavior as the amount of Li vacancy ordering increases.

We also include the effects of tortuosity within the macro-homogenous porous electrode model, not by explicit consideration of electrode particles, but by using an implicit analytical

Table 1
Material parameters used in simulation.

Parameters	Description	Cathode (LiCoO$_2$)	Separator	Reference
h (µm)	Component thickness	Varies based on geometry	25	
$c_{s,max}$ (mol m^{-3})	Maximum concentration of Li + reaction sites	51555		[36]
$c_{s,init}$ (mol m^{-3})	Initial Li + concentration in electrode	25777		[36]
c_0 (mol m^{-3})	Initial electrolyte salt concentration	1000	1000	[36]
D_s (cm^2 s^{-1})	Solid phase diffusion coefficient	9×10^{-13} to 3.0×10^{-10} (varies as a function of state of charge)		[31]
α_a, α_c	Anodic, cathodic charge transfer coefficient	0.5		[36]
r_p (µm)	Particle radius	2		[36]
k_a (m s^{-1})	anodic reaction rate constant	5.0×10^{-7}		[12]
k_c (m s^{-1})	Cathodic reaction rate constant	1.0×10^{-7}		[12]
σ_s (S m^{-1})	Electrical conductivity of solid phase	10		[36]
ε_s	Volume fraction of active material	0.52		[36]
ε_l	Volume fraction of porosity	0.338	0.37	[36]
ε_f	Volume fraction of filler	0.142		[36]
ν	Porosity left by carbon/electrolyte mixture	0.9		Assumed
t_+	Transference number	0.2	0.2	[36]
T (K)	Temperature	298	298	Assumed

relation of the tortuosity (τ) of an assembly of non-porous particles developed by Vijayaraghavan et al. [32]. The Bruggemann relationship ($\tau = \varepsilon_l^{-0.5}$) has been the most widely used tortuosity relationship in macro-homogeneous battery models. However, different materials often have different tortuosity properties and do not always hold to the Bruggemann relationship [33,34]. As a result, a more detailed tortuosity relationship should be used to create a model which can more accurately represent tortuosity effects when the volume fractions of active material, binder, and carbon are varied in the electrode model. The tortuosity of a system has a large impact on lithium-ion diffusion lengths and overall cell capacity. The effective salt diffusivity ($D_{l,eff} = D_l \varepsilon_l / \tau$) and conductivity ($\kappa_{l,eff} = \kappa_l \varepsilon_l / \tau$) of a macroscopic electrode are typically a function of τ, the analytically calculated impact of tortuosity. D_l and κ_l are the intrinsic diffusivities and conductivities, respectively and ε_l is macro-porosity of the homogenous electrode assembly. Equation (15) is used to account for tortuosity in an electrode which has low macroscopic porosity due to large active material particles (LiCoO$_2$) combined with finer carbon conductor particles which increases the overall diffusion path length [32]. The pore space unoccupied by carbon particles in the conductor carbon/electrolyte space is represented by ν. This relationship fits quite well the experimental conductivity data for a large number of synthetic (organic and inorganic) materials made with non-porous beads, over the 0.3 to 1.0 range of porosities [35].

$$\tau = \frac{1}{(\nu \varepsilon_l)^{-0.5}} \tag{15}$$

For all of the models presented in the next section, a structured grid mesh was used with elements sized to 1—2 μm with an aspect ratio of 1. The smallest feature in any given model had a minimum of 10 elements across its boundary. The MUMPS (Multifrontal Massively Parallel) direct solver was used in Comsol 4.3 with maximum time steps limited to 5 s increments with a tolerance factor of 10^{-3}. All models were distributed across two dual Intel Xeon X5650 Hex core Linux cluster nodes with 48 GB of RAM each with a run time around 12—24 h for each case depending on the size of the model.

4. Modeling results and analysis

We analyze the results of modeled co-extruded structures in terms of various design metrics in order to understand how geometrical parameters impact electrode performance. First, we map specific capacity predictions of battery performance against a dimensionless geometric variable (S) by developing an appropriate relationship which relates the cross-section of the electrode pillars with the total perimeter of the electrode (P) and the ratio of the width of LiCoO$_2$ to the electrolyte region spacing. As was previously mentioned in Section 1.1.2, Long et al. [14] developed parameter U which was dependent on the radius (or width) of electrode pillars relative to the overall height or length. We take this parameter one step further and take into account the spacing of the electrode pillars and electrolyte regions as Long's parameter focused on a single electrode pillar interdigitated with an anode. We introduce a dimensionless shape parameter, S, where S is defined by the relationship below:

$$S = \frac{P^2}{A} \cdot \left(\frac{w_{elec}}{w_{LCO}}\right)^2 \tag{16}$$

A is the total cross-sectional area of active material pillars (constant for all designs) and is defined by $A = n w_{LCO} h$. P is the total perimeter of the LiCoO$_2$ pillars exposed to electrolyte and is defined

as $P = n \, (w_{LCO} + 2h)$. (w_{elec}^2 / w_{LCO}^2) is formulated as such to add a dependency on the widths of the electrolyte and electrode regions. For a given h, as the number of electrode pillars, n, is continuously increased, keeping A constant, the shape parameter S is expected to reach a saturation point. We believe this saturation point exists because for very thin pillars diffusion will no longer be the limiting factor in battery performance.

The geometrical parameters h, w_{elec}, and w_{LCO} are varied over a range of dimensions which are feasible with co-extrusion to help us to better understand where a saturation point exists on the specific capacity of a LiCoO$_2$ battery. Fig. 4 shows a plot of dimensionless shape parameter, S, against specific capacity while Table 2 summarizes the dimensions and performance of individual cases at a 1C discharge rate. Fig. 4 shows that, as a function of S there is a limit on expected battery performance for a fixed amount of active material in the LiCoO$_2$ cathodes. The first row in Table 2 represents an industry standard thin porous LiCoO$_2$ cathode modeled based on parameters from Ning et al. [36]. The baseline thin porous electrode case is also represented by the horizontal black dashed line on the plot in Fig. 4. The thin porous electrode case gives us a material utilization comparison point at a 1C rate. The goal for the co-extruded designs is to reach the same specific capacity at a 1C rate in order to achieve maximum material utilization. For the baseline $h = 74$ μm porous electrode case, a 1C current density of 2.0 mAh cm^{-2} is applied. The current is scaled accordingly for the thicker electrode cases with 4.1, 5.4, 8.1 and 10.8 mAh cm^{-2} applied to the 150, 200, 300, and 400 μm thick electrode cases respectively. As one can see, there is an asymptotic trend reaching a saturation point with each electrode pillar height (h) with the 200 μm thick and 150 μm thick cases meeting or slightly surpassing the expected utilization at a 1C rate. The top ranking cases, based on the design parameter S, had electrolyte and electrode regions which were 100 μm in width or less, increasing the amount of electrode surface area exposed to electrolyte. The 300 μm thick electrodes saturate around 98 mAh g^{-1} while the 400 μm thick electrode cases saturate around 92 mAh g^{-1}. Although the 300 and 400 μm thick electrode cases do not reach the same utilization as the 74 μm thick electrode, it is important to note that both of these ultra-thick electrodes substantially beat the utilization rate of their ultra-thick monolithic counterparts by 1.5—5 times (see Table 2).

Looking at the design parameter S, one can see that in order to maximize active material utilization, S should be maximized by increasing the total perimeter (P) of electrode material exposed to electrolyte for a given volume of material. S, however, is not a
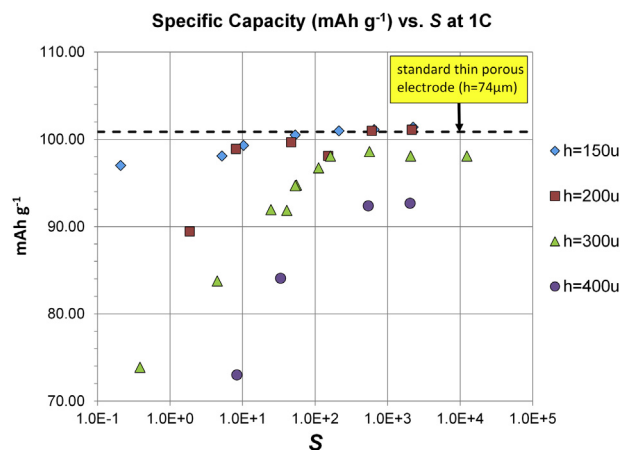

Fig. 4. Plot of dimensionless design parameter, S, against specific capacity at a 1C discharge rate.

Table 2
Geometrical parameters and capacity estimations for co-extruded cathode structures.

h (µm)	w_{elec} (µm)	w_{LCO} (µm)	w_{LCO}/w_{elec}	# of cathode pillars	Total electrode volume (mm^c)	Cathode material volume (mm^c)	S (design parameter)	Specific capacity (mAh g^{-1})	Total electrode capacity (mAh g^{-1})[a]	Volumetric capacity (mAh cm^{-3})[b]
74[c]	n/a	n/a	n/a	n/a	0.30	0.30	n/a	100.86	65.58	262.76
400[c]	n/a	n/a	n/a	n/a	0.30	0.30	n/a	14.42	11.05	37.57
400	25	25	1	30	0.61	0.30	2.04E+03	92.66	50.47	118.72
400	50	50	1	15	0.62	0.30	5.42E+02	92.37	49.85	116.44
400	100	150	1.5	5	0.54	0.30	3.34E+01	84.07	48.98	121.67
400	50	150	3	5	0.42	0.30	8.36E+00	72.99	48.31	135.82
300[c]	n/a	n/a	n/a	n/a	0.30	0.30	n/a	49.04	37.06	127.76
300	50	50	1	20	0.62	0.30	5.63E+02	98.59	52.42	125.29
300	100	100	1	10	0.63	0.30	1.63E+02	98.08	51.43	121.67
300	25	25	1	40	0.61	0.30	2.08E+03	98.08	52.52	126.18
300	10	10	1	100	0.60	0.30	1.24E+04	98.08	52.75	127.12
300	125	125	1	8	0.64	0.30	1.12E+02	96.72	50.37	118.58
300	300	250	0.83	4	0.75	0.30	5.55E+01	94.75	44.70	98.74
300	200	200	1	5	0.66	0.30	5.33E+01	94.69	48.30	112.13
300	200	250	1.25	4	0.60	0.30	2.47E+01	91.94	49.59	119.76
300	50	100	2	10	0.47	0.30	4.08E+01	91.85	56.87	154.37
300	25	125	5	8	0.37	0.30	4.49E+00	83.77	58.07	178.14
300	25	250	10	4	0.34	0.30	3.85E−01	73.86	53.16	171.05
200[c]	n/a	n/a	n/a	n/a	0.30	0.30	n/a	80.77	59.46	210.42
200	25	25	1	60	0.61	0.30	2.17E+03	101.09	52.28	130.60
200	50	50	1	30	0.61	0.30	6.08E+02	100.96	51.95	129.36
200	50	100	2	15	0.46	0.30	4.69E+01	99.66	60.03	169.33
200	100	250	2.5	6	0.44	0.30	8.11E+00	98.88	60.94	175.64
200	25	50	2	30	0.46	0.30	1.52E+02	98.08	59.41	168.47
200	10	100	10	15	0.33	0.30	1.88E+00	89.42	63.03	210.51
150[c]	n/a	n/a	n/a	n/a	0.30	0.30	n/a	92.31	66.24	240.48
150	25	25	1	80	0.60	0.30	2.25E+03	101.38	50.63	131.24
150	50	50	1	40	0.61	0.30	6.53E+02	101.11	50.31	130.08
150	100	100	1	20	0.62	0.30	2.13E+02	100.96	49.86	128.30
150	50	100	2	20	0.46	0.30	5.33E+01	100.49	58.79	171.66
150	100	250	2.5	8	0.44	0.30	1.03E+01	99.29	59.67	178.40
150	50	200	4	10	0.38	0.30	5.21E+00	98.08	62.92	200.40
150	10	200	20	10	0.32	0.30	2.08E−01	96.99	67.99	239.50

[a] Capacity calculation includes the weight of active electrode material, electrode filler material (carbon and binder), electrolyte, and a 20 µm thick aluminum current collector.

[b] Total volume includes the physical space inhabited by both the electrode material and the electrolyte regions.

[c] Monolithic (unstructured) porous electrode comparison.

perfect estimation. If we look at the case where $w_{LCO} = w_{elec} = 10$ µm, S has the highest value of any co-extruded electrode design presented in Table 2. However, at a 1C discharge, the performance of the aforementioned case is not much different from cases where the LiCoO$_2$ and electrolyte regions are 25–100 µm wide.

Although co-extrusion can realize features down to 1 µm, $w_{LCO} = 10$ µm, for the given materials system studied in this paper, is at the practical limit of a real battery structure. The active material particles in the model have a diameter of 4 µm which would in effect mean no more than two particles could lie across the width of the LiCoO$_2$ regions. If these narrow structures were fabricated with a battery ink, in actuality there would be a Gaussian distribution of particle diameters where particles may be substantially larger or smaller than 4 µm introducing potential problems with particle alignment in co-extruded features which are 10 µm or smaller. The $w_{LCO} = 10$ µm case was simulated to check if theoretically finer features could help realize better utilization in thick electrodes, but since the result was no better than the cases where $w_{LCO} = w_{elec} = 25$ µm, the $w_{LCO} = 10$ µm case was only studied for the 300 µm thick electrode. This proves that no future gains due to diffusivity through thinner (<25 µm) electrode features are expected at the 1C discharge rate being considered.

Another interesting parameter to examine is how the relative width of the pillars (w_{LCO}) and electrolyte regions (w_{elec}) impacts the specific capacity and total capacity of the co-extruded half-cell geometries. Based on the results presented in Fig. 5a, designs which have matched widths ($w_{LCO} = w_{elec}$) have the best material utilization at a 1C rate. Narrow electrolyte regions, where $w_{LCO}/w_{elec} \geq 2$, are largely unfavorable in the 200–400 µm thick electrodes. Whereas Fig. 5a, looks at specific capacity based on active material only, Fig. 5b looks at the total electrode capacity at 1C, taking into account the weight of the electrode filler material, electrolyte, and current collector. $w_{LCO}/w_{elec} \geq 2$ is favored in this case as narrower electrolyte channels add less weight to the overall electrode design. The co-extruded design with $h = 150$ µm, $w_{LCO} = 200$ µm, and $w_{elec} = 10$ µm is the best performing design in Fig. 5b.

When comparing Figs. 5a and 6, a trade-off between volume and material utilization can be seen. Looking at Fig. 6, which examines the ratio of the feature widths to the total electrode volumetric capacity, one can see $w_{LCO}/w_{elec} > 1$ is favored on a volumetric basis. To illustrate this point, the capacity numbers in Fig. 6 are calculated based on the entire cathode volume (including the electrolyte regions). Larger width electrolyte regions penalize the overall cell capacity as one needs to grow the cell volume to account for the electrolyte regions which fundamentally enable better Li$^+$ transport in thick electrodes. Although for $w_{LCO}/w_{elec} > 2$, non-optimal specific capacity is observed in the thicker electrode models, the electrolyte channels still enable the ultra-thick electrodes to perform substantially better than their equivalent thickness monolithic counterparts (see Table 2). Active material utilization in
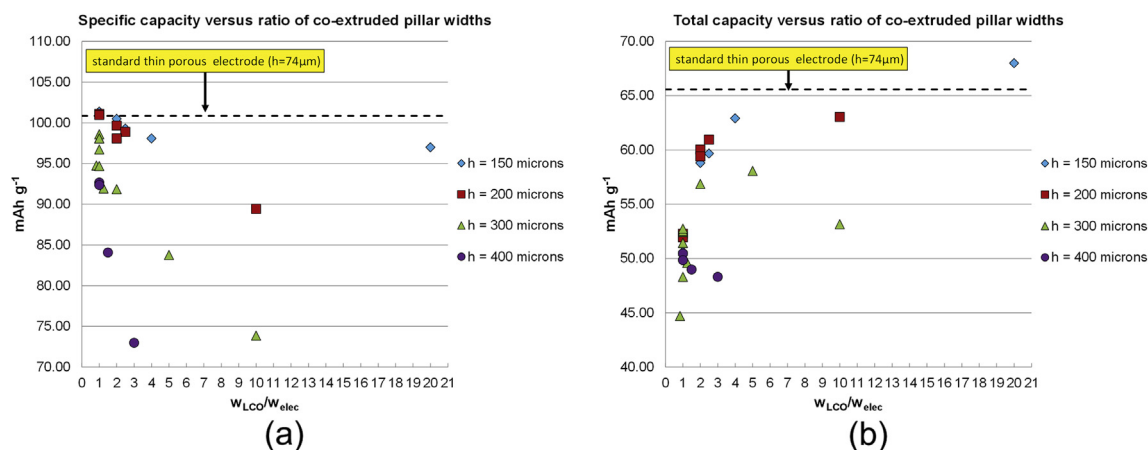
Fig. 5. Plot of specific capacity (a) and total capacity (b) against the ratio of LiCoO$_2$ and electrolyte region widths.

thick electrodes favors cases where $w_{LCO} = w_{elec}$, however because electrolyte pillars add additional volume and weight for electrolyte, if one desires minimizing the total weight or volume of a system, cases where w_{elec} is substantially smaller than w_{LCO} are favored.

When examining the results in Figs. 5 and 6, one must also consider the fact that we are only examining single battery layers when in actuality, these electrodes will be included in multi-layer prismatic or wound cell assemblies where the thicker electrodes will enable the removal of multiple separator ($\sim$25 μm) and current collector layers ($\sim$20 μm for each anode and cathode). As an example, if one makes a cell with multiple layers of the baseline cell (current collectors, separator, anode, and a standard 74 μm thick cathode), a similar stack could be made with a co-extruded design but fewer layers (on the order of 40–75% less) would be required overall to reach the same target cell capacity, meaning almost a 10–30% reduction in inactive cell assembly components (depending on the carbon anode thickness) for co-extruded structures in the 150–300 μm thickness range. Depending on the format and operating discharge rate, battery stack integration can substantially change the expected energy density output of the co-extruded designs presented in this paper.

Fig. 7 shows normalized lithium utilization surface plots (where 1 indicates full utilization of the active electrode material and 0.8 indicates only 80% utilization of the active material) for three different electrode thicknesses for a fixed electrode and electrolyte

Fig. 6. Plot of volumetric capacity for the entire cathode electrode against the ratio of pillar widths.

region width of 25 μm. One can see in the plot for $h = 400$ μm, almost half of the electrode is not fully utilized at a 1C rate whereas the 200 μm case realizes essentially full utilization. Relative to standard batteries, co-extrusion greatly reduces the distances over which Li$^+$ transport must occur. However, there is a transition point where for a large enough height of the electrode (h), in a given materials system, ohmic loses will begin to dominate, reducing any performance improvement.

Looking at Fig. 8, one can see that in the two cases where $w_{LCO} > w_{elec}$, a larger lithium and electrolyte salt gradient is observed at the end of a 1C discharge. This larger gradient means higher current density is required in the electrode and in turn higher current densities yield higher overpotentials causing a cell to reach its cut-off potential sooner than expected. From a specific capacity and material utilization viewpoint, the modeling results demonstrate that narrow electrolyte channels in relation to the active material pillars limit Li$^+$ transport, and thus ultra-thick co-extruded pillars favor cases where $w_{elec} \geq w_{LCO}$. Looking at Fig. 8 and Table 2, overall the finer width co-extruded cathode features yield the highest specific capacity at 1C.

As we advance towards manufacturing these new co-extruded electrode architectures, attention must be paid to non-uniformities which can arise and potentially cause cell failures. Non-uniform current densities typically cause lower cell efficiencies and non-uniform heating within the cell. Fundamentally, Li$^+$ transport becomes anisotropic in structured 3D electrodes and current flow is no longer one dimensional and uniform. Looking at Fig. 9, an interesting phenomenon is observed. High current density spikes in the liquid phase of the battery are seen at the corners of the co-extruded stripes which contact the separator. All of the models presented so far have assumed ideal rectangular cross-sections for the co-extruded features. However, with co-extrusion, we can tune the cross-sectional geometry of the cathode material by varying print speeds, ink viscosities, and the fluidic path of the printhead. If we take one of the better performing electrode cases, where $h = 200$ μm and $w_{elec} = w_{LCO} = 25$ μm, and round the corners of the structures and slightly extend the base to form a trapezoid like structure, while still conserving mass in the design, a minimized current density distribution results at the end of a 1C discharge. For both cases, the current density is higher at the edges of the electrode which meet the separator than in the center of the pillar, leading to a non-uniform current distribution in the electrolyte phase. Fig. 9, shows that by rounding sharp features in the electrode structures, the corner concentration effects can be minimized. Further work is required to investigate the corner
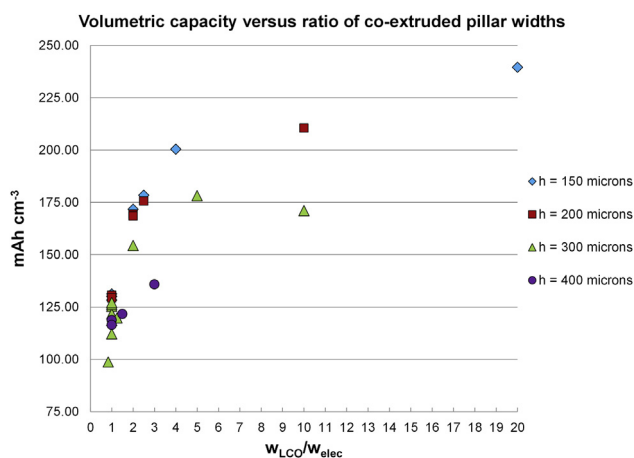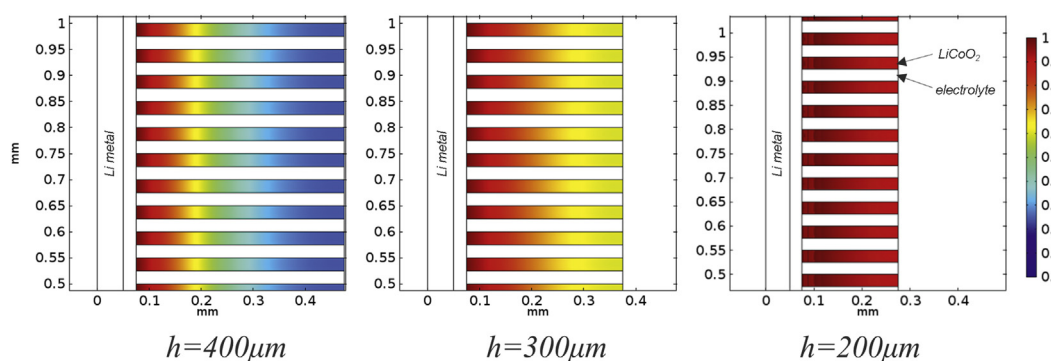
Fig. 7. Normalized Li$^+$ utilization plots at the end of a 1C discharge. All cases have $w_{LCO} = w_{elec} = 25$ μm. Full utilization at narrowest co-extruded width features is reached with 200 μm or shorter pillars.

effects of the electrodes in order to better understand what is fundamentally an effect of the geometry and material versus underlying model assumptions.

We are currently in the process of fabricating these structures and additional variations on the geometry and material formulations in order to compare the model and experiment. In addition, we will use the comparison to understand potential failure modes over the cycle life of a battery which are difficult to capture in a model without experimental data.

5. Conclusions

In this paper, we have presented modeling results for a novel battery electrode structure which can be fabricated with co-extrusion technology developed at PARC (Palo Alto Research Center). Utilizing material parameters from an existing LiCoO$_2$ cathode design and John Newman's macro-homogeneous porous electrode model, we conducted a series of electrochemical models to understand how co-extruded electrode structures enable better material utilization in ultra-thick electrodes. With the chosen LiCoO$_2$ materials system, co-extruded features which are 25–100 μm in width gave the best active material utilization at a 1C rate for electrode thicknesses in the range of 150–300 μm. Co-extruded electrode structures fundamentally minimize the ionic pathway for lithium ions. Electrons and ions have to travel shorter physical distances in the co-extruded structures, enabling electrode heights which are 2–5 times greater than conventional cells. For the particular co-extruded structure embodiment studied, electrolyte channels which were similar in width to the active material pillars yielded the best utilization results. We also found that the addition
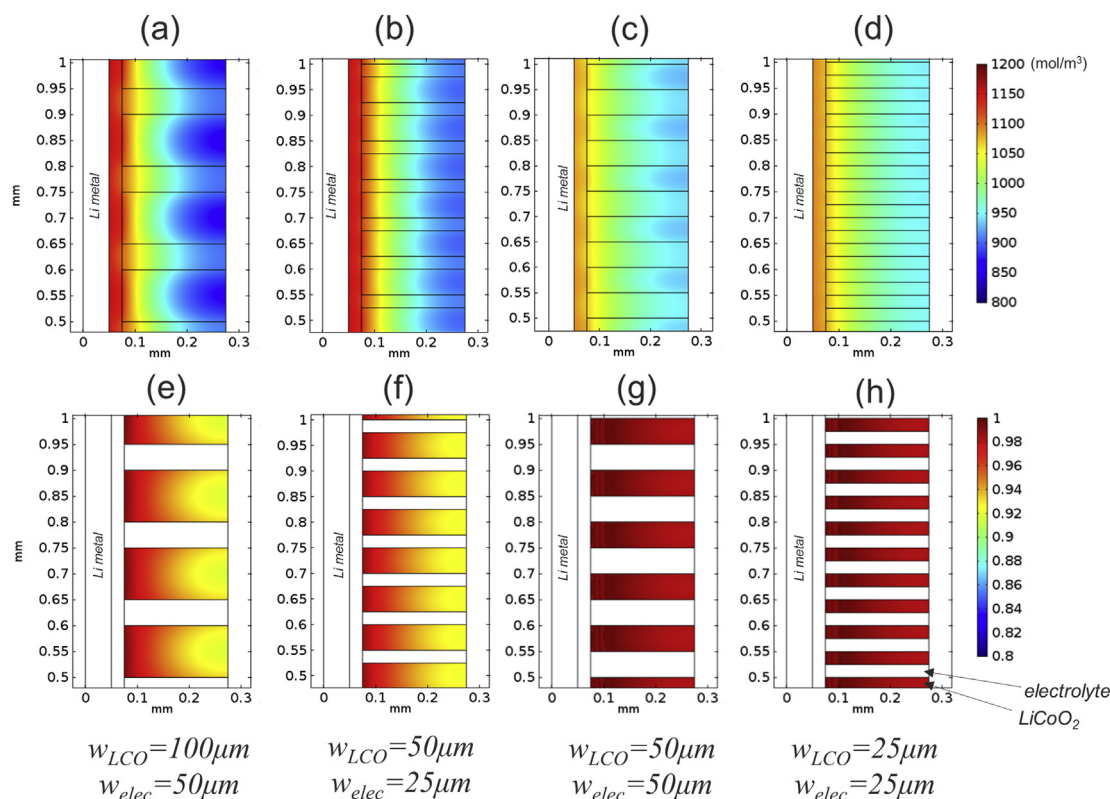

Fig. 8. Four co-extruded structures with a fixed cathode height of 200 μm are shown above. (a)–(d) show electrolyte salt concentration profiles while (e)–(h) show Li$^+$ utilization plots normalized by the maximum concentration in the material at the end of a 1C discharge.
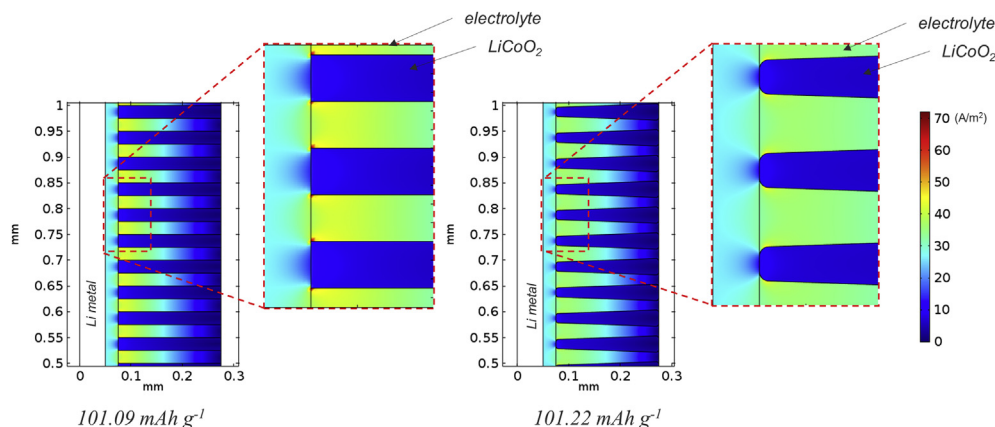
Fig. 9. Electrolyte phase current density distribution at the end of a 1C discharge. Both electrodes are 200 μm thick. The image on the left is the $w_{elec} = w_{LCO} = 25$ μm case study with ideal rectangular cross section electrodes (maximum current density observed is 71.8 A m^{-2}). The image on the left is a trapezoidal geometry with rounded corners and maintaining the same cross-sectional area as the case on the left (maximum current density observed is 48.1 A m^{-2}).

of large electrolyte channels to an electrode impacts the overall energy density of a cell as additional volume and weight must be added to the electrode. However, battery stack level performance estimations should be made in the future to truly understand the volume and weight penalties electrolyte channels have on overall battery stack design.

Looking forward, although a standard EC:PC:DMC electrolyte was used for the study in this paper, more conductive electrolytes which garner even better material utilization in thick electrodes or polymer gel electrolytes which can enable structural support between the electrode pillars are two areas that require further exploration. Additional material systems, including graphitic anodes, can benefit from the co-extruded geometries presented in this paper. Although each material system is different, if we moved from LiCoO$_2$ to LiMnO$_2$ (Lithium-manganese dioxide), as an example, we believe co-extrusion will help increase the performance of a new material and enable thicker than standard electrodes. Since different electrode materials have different diffusion properties and grain sizes, the optimal structures found for one material system may not be the optimal structures for another material system. A systematic search will need to be conducted again, but the model presented in this paper can help provide the answers for a large class of related materials. Moreover, creating a more generalized design table or a series of design relationships for co-extruded parameters where the active material particle size, porosity, and conductivity are also varied would further enable us to understand under which conditions certain electrode structures will benefit the most.

Acknowledgments

References

[1] M. Wakihara, Mater. Sci. Eng. R. 33 (2001) 109–134.
[2] J.B. Bates, N.J. Dudney, D.C. Lubben, G.R. Gruzalski, B.S. Kwak, X.H. Yu, R.A. Zuhr, J. Power Sources 54 (1995) 58–62.
[3] J.H. Pikul, H.G. Zhang, J. Cho, P.V. Braun, W.P. King, Nat. Commun. 4 (2013) 1732.
[4] K. Evanoff, J. Khan, A.A. Balandin, A. Magasinski, W.J. Ready, T.F. Fuller, G. Yushin, Adv. Mater. 24 (2012) 533–537.
[5] S.T. Lee, S.W. Jeon, B.J. Yoo, S.D. Choi, H.J. Kim, S.M. Lee, J. Power Sources 155 (2006) 375–380.
[6] N.J. Dudney, Y.I. Jang, J. Power Sources 119-121 (2003) 300–304.
[7] K.A. Littau, C.L. Cobb, N. Spengler, S. Solberg, M. Weisberg, N. Chang, A. Rodkin, in: Proc. SPIE, Micro- and Nanotechnology Sensors, Systems, and Applications III, vol. 8031, 2011.
[8] C.C. Ho, K. Murata, D.A. Steingart, J.W. Evans, P.K. Wright, J. Micromech. Microeng. 19 (2009) 094013.
[9] L. Baggetto, J.F.M. Oudenhoven, T. van Dongen, J.H. Klootwijk, M. Mulder, R.A.H. Niessen, M.H.J.M. de Croon, P.H.L. Notten, J. Power Sources 189 (2009) 402–410.
[10] L. Baggetto, H.C.M. Knoops, R.A.H. Niessen, W.M.M. Kessels, P.H.L. Notten, J. Mater. Chem. 20 (2010) 3703–3708.
[11] C.-J. Bae, C.K. Erdonmez, J.W. Halloran, Y.-M. Chiang, Adv. Mater. 25 (2013) 1254–1258.
[12] R.E. Garcia, Y.M. Chiang, J. Electrochem. Soc. 154 (2007) A856–A864.
[13] V. Zadin, H. Kasemägi, A. Aabloo, D. Brandell, J. Power Sources 195 (2010) 6218–6224.
[14] J.W. Long, B. Dunn, D.R. Rolison, H.S. White, Chem. Rev. 104 (2004) 4463–4492.
[15] V. Zadin, D. Brandell, H. Kasemagi, A. Aabloo, J.O. Thomas, Solid State Ionics 192 (2011) 279–283.
[16] M. Smith, R.E. Garcia, Q.C. Horn, J. Electrochem. Soc. 156 (2009) A896–A904.
[17] M. Roberts, P. Johns, J. Owen, D. Brandell, K. Edstrom, G.E. Enany, C. Guery, D. Golodnitsky, M. Lacey, C. Lecoeur, H. Mazor, E. Peled, E. Perre, M.M. Shaijumon, P. Simon, P.-L. Taberna, J. Mater. Chem. 21 (2011) 9876–9890.
[18] C. Simonnet, A. Groisman, Appl. Phys. Lett. 87 (2005) 114104-1–114104-3.
[19] T. Stiles, R. Fallon, T. Vestad, J. Oakey, D.W.M. Marr, J. Squier, R. Jimenez, Microfluid. Nanofluid. 1 (2005) 280–283.
[20] M. Park, X. Zhang, M. Chung, G.B. Less, A.M. Sastry, J. Power Sources 195 (2010) 7904–7929.
[21] COMSOL 4.3 software: http://www.comsol.com/.
[22] M. Doyle, T.F. Fuller, J. Newman, J. Electrochem. Soc. 140 (1993) 1526–1533.
[23] T.F. Fuller, M. Doyle, J. Newman, J. Electrochem. Soc. 141 (1994) 1–10.
[24] T.F. Fuller, M. Doyle, J. Newman, J. Electrochem. Soc. 141 (1994) 982–990.
[25] M. Doyle, J. Newman, J. Power Sources 54 (1995) 46–51.
[26] J.S. Newman, K.E. Thomas-Alyea, Electrochemical Systems, third ed., Prentice-Hall, Eaglewood Cliffs, NJ, 2004.
[27] V. Ramadesigan, P.W.C. Northrop, S. De, S. Santhanagopalan, R.D. Braatz, V.R. Subramanian, J. Electrochem. Soc. 159 (2012) R31–R45.
[28] K. Mizushima, P.C. Jones, P.J. Wiseman, J.B. Goodenough, Mater. Res. Bull. 15 (1980) 783–789.
[29] Q. Zhang, Q. Guo, R.E. White, J. Power Sources 165 (2007) 427–435.
[30] L.O. Valoen, J.N. Reimers, J. Electrochem. Soc. 152 (2005) A882–A891.
[31] Y.-I. Jang, B.J. Neudecker, N.J. Dudney, Electrochem. Solid-State Lett. 4 (2001) A74–A77.
[32] B. Vijayaraghavan, D.R. Ely, Y.M. Chiang, R. García-García, R.E. García, J. Electrochem. Soc. 159 (2012) A548–A552.
[33] M. Doyle, J. Newman, A.S. Gozdz, C.N. Schmutz, J.-M. Tarascon, J. Electrochem. Soc. 143 (1996) 1890–1903.
[34] M. Doyle, Y. Fuentes, J. Electrochem. Soc. 150 (2003) A706–A713.
[35] M. Barrande, R. Bouchet, R. Denoyel, Anal. Chem. 79 (2007) 9115–9121.
[36] G. Ning, R.E. White, B.N. Popov, Electrochim. Acta 51 (2006) 2012–2022.